


Article

Glass-Forming Ability, Chemical Durability, and Structural Properties of Lead Dioxide-Silicate Glass System

Mioara Zagrai ¹, Radu Cristian Gavrea ¹, Sergiu Macavei ¹ , Adriana Augusta Dehelean ¹, Adriana Popa ¹, Maria Loredana Soran ¹  and Raluca Anca Mereu ^{2,*} 

¹ National Institute for Research and Development of Isotopic and Molecular Technologies, 400293 Cluj-Napoca, Romania; mioara.zagrai@itim-cj.ro (M.Z.)

² Faculty of Chemistry and Chemical Engineering, Babes-Bolyai University, 11 Arany Janos Street, 400084 Cluj-Napoca, Romania

* Correspondence: raluca.mereu@ubbcluj.ro

Abstract: The present study aimed to test the solubility of SiO₂ in a PbO₂ host glass matrix. The new glass system with chemical composition xSiO₂·(100-x)·PbO₂ (in mol%) was obtained at low temperature using the melt-quenching technique. The method proposed for the characterization of the glass system includes X-ray diffraction (XRD), Differential Scanning Calorimetry (DSC), inductively coupled plasma mass spectrometry (ICP-MS), Fourier Transform Infrared (FTIR), and Electron Spin Resonance (ESR) spectroscopy. Understanding the relationship between the oxide composition, structure, chemical durability, and thermal characteristics of obtained materials is essential for further developing the new glass crystalline material (GCM) compositions with specific desired properties.

Keywords: lead-silicate glass; thermal proprieties; chemical durability; structural properties; glass crystalline materials



Citation: Zagrai, M.; Gavrea, R.C.; Macavei, S.; Dehelean, A.A.; Popa, A.; Soran, M.L.; Mereu, R.A. Glass-Forming Ability, Chemical Durability, and Structural Properties of Lead Dioxide-Silicate Glass System. *Crystals* **2024**, *14*, 436. <https://doi.org/10.3390/cryst14050436>

Academic Editor: Yael Diskin-Posner

Received: 8 April 2024

Revised: 28 April 2024

Accepted: 2 May 2024

Published: 4 May 2024



Copyright: © 2024 by the authors. Licensee MDPI, Basel, Switzerland. This article is an open access article distributed under the terms and conditions of the Creative Commons Attribution (CC BY) license (<https://creativecommons.org/licenses/by/4.0/>).

1. Introduction

Nowadays, there is a pressing demand for the development of novel materials possessing specific properties tailored to meet diverse industrial requirements. One area of particular focus is glass crystalline materials, which hold significance for their unique combination of amorphous and crystalline characteristics within a single substance [1]. These materials, referred to as glass crystalline materials (GCMs), are composite materials comprising both vitreous (glassy) and crystalline phases [2]. They are typically fabricated through either low-temperature sintering using precursors consisting of glass frit, oxides, and crystalline phases, or conventional melting followed by controlled crystallization of a parent glass [3].

The distinctive properties of GCMs render them increasingly vital across various practical applications such as photonics, optoelectronics, energy storage, and environmental waste management. Crystallization in glass entails the transformation of the disordered atomic structure of a glass system into a well-ordered crystalline structure. This process involves two primary mechanisms: nucleation and crystal growth, which can occur through either surface or volume crystallization. These mechanisms are heavily influenced by the viscosity of the molten glass, which is dictated by the initial composition of the glass [4]. Crystallization and nucleation processes depend not only on the viscosity of the supercooled liquid, but also on the intermolecular interaction and thermodynamic driving force [5].

In the processing of GCMs, it is important to understand the structural and behavioral evolution of the starting glass composition that is intended for use in the successful development of a GCM for a specific application. Then, complex characterization of these materials to understand their properties is essential.

Glass compositions incorporating heavy metal elements like lead exhibit a range of distinctive characteristics and intriguing properties. These include elevated refractive

indices, infrared (IR) transparency, and nonlinear optical attributes, all of which hold significant promise in the realms of photonics and optoelectronics. Lead oxide-containing glasses find wide-ranging applications spanning crystal glasses, enamels, and glazes, to optical glasses characterized by high refractive indices. Moreover, they are utilized in glasses designed to absorb ionizing radiation, as well as in glasses employed for the low-temperature welding of metals, ceramics, or other glasses [6–8]. PbO_2 holds significance in glass compositions owing to its capacity to establish both covalent and ionic bonds with oxygen ions [9,10]. This exceptional property stems from their dual role as both network-modifying and network-forming entities, rendering them particularly appealing for specialized optical glass applications [11–13]. The fabrication process for Heavy Metal Oxide Glasses (HMOGs) is straightforward, facilitated by the comparatively expansive glass-forming region. Moreover, binary network-forming glasses exhibit outstanding optical, thermal, and mechanical properties, making them immensely valuable for a multitude of applications in electronics, optoelectronics, and the storage of nuclear waste [14]. A notable subset of binary network-former glasses revolves around the lead–silicate system. Within silicate glass, lead functions as a modifier, particularly at lower concentrations. Here, Pb^{2+} ions integrate into areas containing alkaline ions, where they interact with non-bridging oxygen atoms. Conversely, at higher PbO_2 concentrations, lead establishes its own glass network, characterized by Pb–O–Pb linkages, serving as a hallmark of network formation and extension by lead. Within these glass matrices, Pb^{2+} ions maintain their stereo-chemically active free $6s^2$ pair and occupy highly asymmetric sites, akin to their counterparts in crystalline phases [15].

Understanding the relationship between oxide composition, structure, chemical durability, and thermal characteristics is essential for further developing new glass compositions with specific desired properties. In this regard, the study aims to obtain, by melt-quenching technique, and investigated structural and behavioral evolution of lead-silicate glasses through, X-ray diffraction (XRD), Differential Scanning Calorimetry (DSC), Inductively Coupled Plasma Mass Spectrometry (ICP-Ms), Fourier Transform Infrared (FTIR), and Electron Spin Resonance (ESR) spectroscopy.

2. Experimental Methods

Lead-silicate glass system with chemical formula of $x\text{SiO}_2(100-x)\cdot\text{PbO}_2$ (in mol%), labeled as PSn where $n = 0\text{--}9$, was obtained by melt-quenching method using as raw materials high-chemical-purity oxide powders: Silicon(IV) oxide, 99.5%, Alfa Aesar, CAS 14808-60-7; and Lead(IV) oxide, 97%, Alfa Aesar, CAS 1309-60-0. The chemical compositions and designed samples are summarized in Table 1. The homogenized mixture of sample batch of 10 grams for each sample was melted, in air atmosphere, in an electrically heated furnace at temperatures ranging from 950 °C to 1050 °C as a function of SiO_2 content for 15 min using platinum crucibles. The melts were fast quenching, at room temperature by pouring onto stainless-steel plate; and, further, the samples were mechanically grinded in an agate mortar to obtained fine powder and used for investigations. The samples were mechanically ground in an agate mortar to obtain fine powder and used for investigations.

Table 1. Composition of the oxide system $x\text{SiO}_2\cdot(100-x)\text{PbO}_2$.

Chemical Composition of the System [% mol] and Sample Codes										
	PS 0	PS 1	PS 2	PS 3	PS 4	PS 5	PS 6	PS 7	PS 8	PS 9
PbO_2	100	90	80	70	60	47	45	42	40	38
SiO_2	0	10	20	30	40	53	55	58	60	62
Processing temperature										
	950 °C					1050 °C				

The structural, thermal, and chemical properties of the new vitreous system were investigated through X-ray diffraction (XRD), Differential Scanning Calorimetry (DSC), Fourier Transform Infrared (FTIR), Electron Spin Resonance (ESR) spectroscopy, and Inductively Coupled Plasma Mass Spectrometry (ICP-MS). The XRD measurements of the glass powder were carried out on a Rigaku SmartLab automated multipurpose X-ray Diffractometer with Cu-K α radiation, operating at 45 kV and 200 mA and using a D/tex Ultra 250 high-speed position-sensitive detector (Rigaku, Tokyo, Japan). Thermal measurements were performed employing an SDTQ600 TA Instrument (TA Instruments, New Castle, DE, USA) thermal analyzer. The thermal analysis was carried out on samples of about 25 mg placed in alumina crucibles, non-isothermally heated up to 1000 °C, with a heating rate of 10 C·min^{−1} in dynamic air-flow atmosphere. The melting and crystallization enthalpies were determined with TA Universal Analysis program by linear integrating peaks. The FTIR absorption spectra of investigated samples were obtained using the JASCO FTIR 6200 spectrometer with resolution ± 2 cm^{−1} and KBr pellet technique (Jasco, Tokyo, Japan). ESR spectra of powder samples were recorded using a Bruker E-500 ELEXSYS spectrometer (Karlsruhe, Germany). The measurements were conducted at room temperature in both X-band (9.52 GHz) and Q band (33.9 GHz), microwave power 2 mW, modulation frequency of 100 kHz. The chemical durability tests were made in duplicate and the estimated values are their average value. ICP-MS was used to analysis the leaching solutions and determine the concentrations of the Pb.

3. Results and Discussion

In Figure 1, images of the obtained samples are presented, captured using a DELTA SMART PRO5 MP digital microscope. Samples PS0-PS4 were obtained at a temperature of 950 °C, while, due to the increasing viscosity of the melt with the progressive increase in SiO₂, the synthesis of samples PS5-PS9 was conducted at 1050 °C. Transparent samples were obtained, with the exception of sample PS5, which is partially slightly opaque, and their color changes from intense orange to colorless as the SiO₂ content increases. Additionally, small bubbles can be observed within the structure of samples PS6-PS9, suggesting the non-homogenization of the composition. To highlight the structure of the obtained samples, they were investigated using XRD.

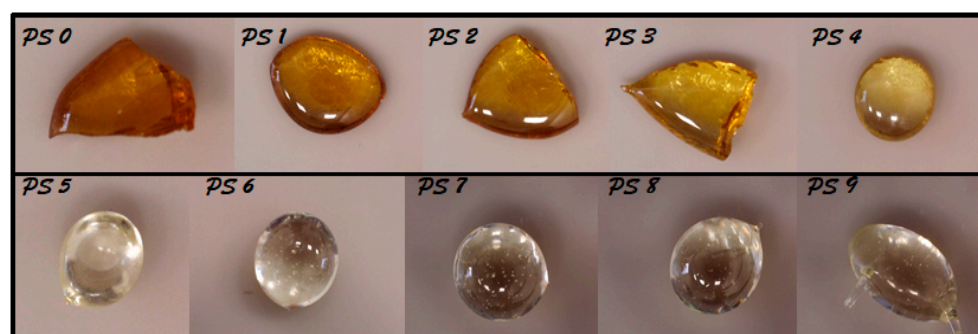


Figure 1. Images of the obtained samples for the PS system.

In Figure 2, XRD patterns for the glassy system with the composition $x\text{SiO}_2 \cdot (100-x)\text{PbO}_2$ are illustrated. The XRD patterns of the samples highlight the presence of broad peaks, associated with an amorphous structure and a disorder structure, respectively.

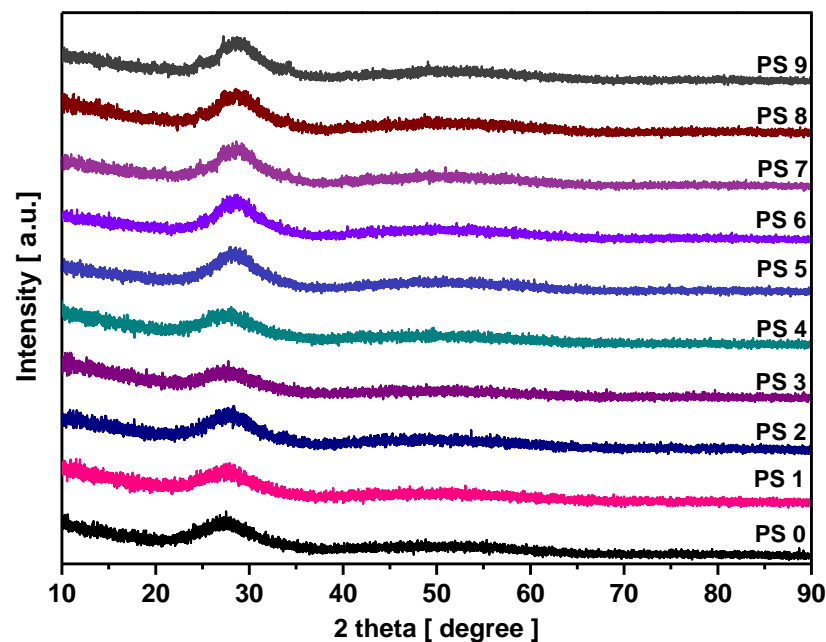


Figure 2. The XRD patterns for the $x\text{SiO}_2 \cdot (100-x) \text{PbO}_2$ system.

A chemical durability test was applied only for free-bubble glass samples, PS0-PS5, respectively. The term “chemical durability” in glass typically refers to the material’s resistance against water, acids, or other aqueous solutions, as well as gases such as water vapor or carbon dioxide present in the atmosphere. The chemical composition of the system, the attacking medium, temperature, and immersion duration are the main factors in evaluating chemical durability or the corrosion mechanism of materials. In this context, the relative chemical durability of the obtained samples underwent testing in accordance with ASTM C1220-98 “Standard Test Method for Static Leaching of Monolithic Waste Forms for Disposal of Radioactive Waste” utilizing the Materials Characterization Centre test 1, MCC 1, method on solid samples. The surface area (SA) of the samples was determined by measuring their geometric surface area using a Roth brand digital caliper. Subsequently, the samples were immersed in distilled water within a sealed polyethylene container, maintaining a consistent surface area-to-volume ratio (S/V) of 10 m^{-1} across all samples.

The samples were kept at a controlled temperature of 90°C in an oven for a period of 7 days. Mass loss was measured by the drying and precise weighing of the samples before and after dissolution. The dissolution rate of the samples (DR) was evaluated from the mass loss after the 7 days (ΔW), the surface area of the sample (SA), and the immersion time (t), applying the following formula:

$$\text{DR} = \frac{\Delta W(\text{g})}{\text{SA}(\text{cm}^2) * t(\text{min})} \quad (1)$$

In Figure 3, the graphs illustrate a) the mass loss and b) the dissolution rate of the samples based on the chemical composition of the system after 7 days of sample immersion. The examination of the results reveals a gradual decrease up to sample PS2, succeeded by a sudden increase for samples PS3-PS6. The dissolution rate for the studied samples ranges between $1.98 \times 10^{-9} \text{ g/cm}^2/\text{min}$ and $6.98 \times 10^{-9} \text{ g/cm}^2/\text{min}$, with the lowest value obtained for sample PS2. The obtained values indicate a relatively low dissolution rate for all samples, and compared to lead-phosphate glasses reported in the literature as matrices for radioactive waste, they are lower by almost three orders of magnitude [16].

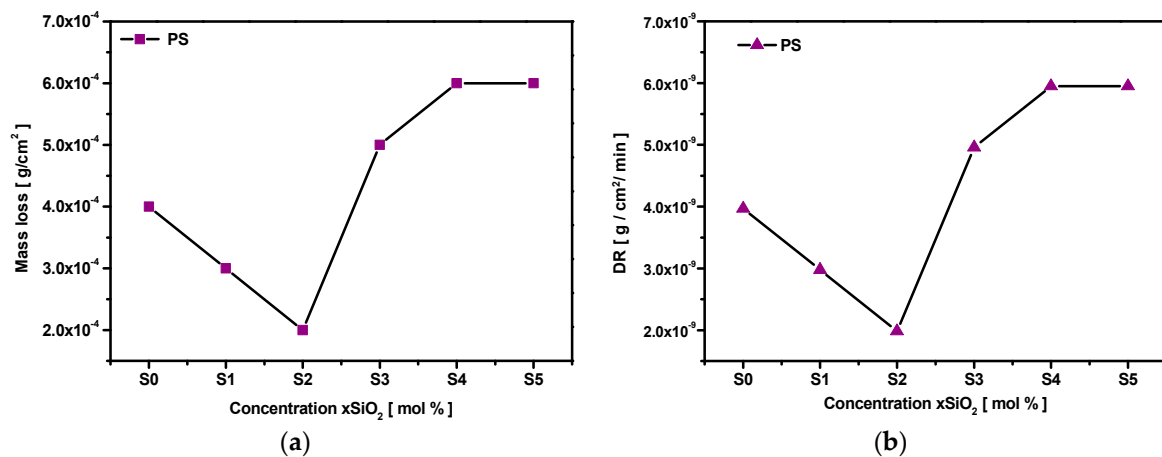


Figure 3. (a) Mass loss and (b) dissolution rate of samples PS0-PS6.

Therefore, from a compositional design perspective, doping the PbO₂-based matrix with SiO₂, specifically sample PS2, is considered the optimal concentration for enhancing the chemical durability of PbO₂-based glass.

In Figure 4, images of the samples immersed in distilled water after a period of 7 days are depicted. The formation of a protective layer on the surface of the samples is evident, although the extent of coverage of this layer varies depending on the chemical composition of the system.

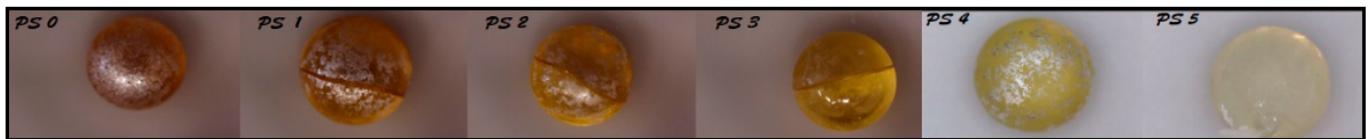


Figure 4. Images of the samples immersed in distilled water after a period of 7 days.

Sample PS0 exhibits the highest coverage, which gradually decreases with increasing SiO₂ concentration up to sample PS2, while for samples PS3 and PS5, this protective layer is nearly invisible. The development of a protective layer that covers the surface of the glass can act as a corrosion inhibition barrier, decreasing the rate of ion inter-diffusion and halting hydrolysis reactions, thereby resulting in a reduced dissolution rate [17]. Samples PS4 and PS5 exhibit chemical reactions resulting in the formation of both a protective layer and the precipitation (opacity) of the samples.

Elemental analysis of the metal content, specifically Pb, in the solution after 7 days was performed using Inductively Coupled Plasma Mass Spectrometry (ICP-MS). The reported analytical results for the Pb concentration (mg/L) represent the average of three distinct measurements. To evaluate the Pb concentration in the samples, normalization of the migrated elemental mass (leaching rate) LR_i was performed. LR_i can be expressed according to the equation below:

$$LR_i = \frac{C_i * V}{S * f_i * t} \quad (2)$$

where LR_i represents the normalized leached (migrated) mass of the element (g/m⁻²/d⁻¹); C_i is the concentration of the element in the solution (g/L); V represents the volume of the solution, i.e., distilled water; S is the surface area of the sample (m²); f_i is the mass fraction of the element in the sample; and t is the immersion time (days). The obtained LR_{Pb} values (g/m⁻²/d⁻¹) corresponding to the chemical composition of the system are outlined in Table 2. It can be noticed that the LR_{Pb} values increase with decreasing PbO₂ concentration in the samples but are maintained at the order of magnitude of 10⁻⁴ g/m⁻²/d⁻¹. The

maximum value was obtained for sample PS3. The obtained values indicate excellent water resistance of the samples and exhibit superior properties compared to lead-borate glasses, which are matrices tested for simulating radioactive waste reported in the literature [18].

Table 2. LR_{Pb} values as a function of the chemical composition of the system.

Normalized Migrated Mass, g/m^2	Chemical Composition of the System					
$LR_{Pb} (g/m^2) \times 10^{-4}$	PS0	PS1	PS2	PS3	PS4	PS5
	2.57	2.83	3.52	5.14	4.13	4.9

The thermal behavior of the obtained samples was investigated through DSC analysis. In Figure 5, the DSC curves for the PS0–PS4 samples are graphically represented. The exothermic effects associated with the crystallization temperature of the samples, T_c ; the endothermic reactions characteristic of the transition temperature, T_g ; the melting temperature, T_m ; and the last endothermic reactions occurring with increasing temperature are summarized in the table below. A nonlinear increase in the T_g values with increasing SiO_2 concentration can be observed, with the T_g value ranging between 363–379 °C. The increase in T_g values may be related to the formation of Si–O–Pb bonds and progressive replacement of weaker Pb–O bonds (101 kJ/mol) with stronger Si–O (443 kJ/mol) bonds.

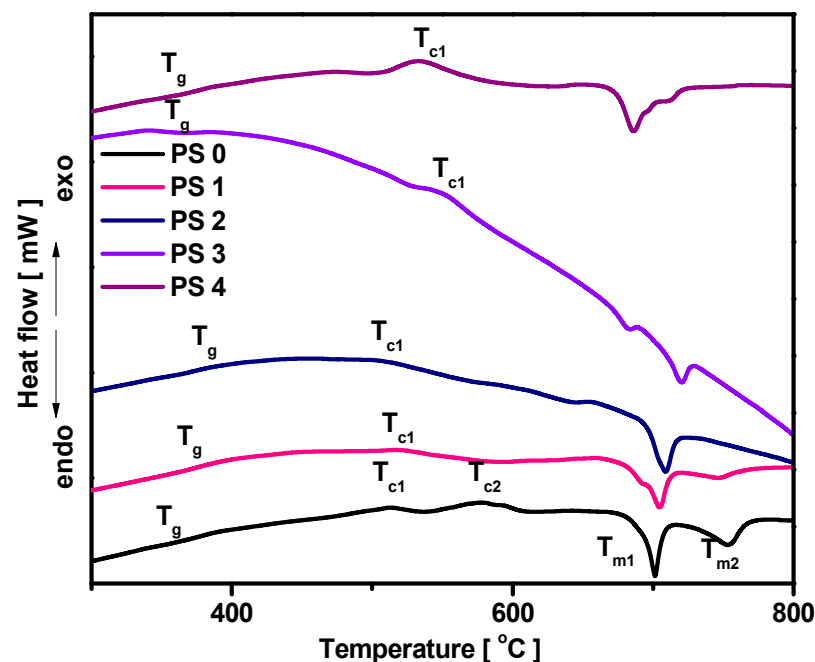


Figure 5. DSC curves of the studied system.

Under the experimental conditions (measurements were conducted in air), the DSC curves of the samples PS5–PS9 are too broad, and endothermic or exothermic events cannot be clearly identified. The thermal stability, ΔT , of materials is evaluated from the difference between T_c and T_g . A value greater than 100 °C represents good thermal stability. For samples PS0–PS4, the ΔT values range from 130 to 173 °C. Also, Weinberg parameter, $K_W = T_c - T_g/T_m$; Hrubby parameters, $K_H = T_{c \text{ onset}} - T_g/T_m - T_{c \text{ onset}}$; and Lu and Liu parameters, $K_{LL} = T_{c \text{ onset}}/T_g + T_m$ were determinate in accordance with ref [19] to evaluate the glass-forming ability of the samples. The obtained values are displayed in Table 3. A high value indicates high stability against crystallization on heating and high ability of glass to vitrify on cooling [19].

Table 3. Thermal parameters for the glassy system.

Thermal Parameters (°C)	Sample				
	PS 0	PS 1	PS 2	PS 3	PS 4
T _g	363	372	379	367	368
T _c	512	518	509	540	538
T _{c onset}	474	490	478	529	502
T _m	701	704	709	682	686
ΔT	149	146	130	173	170
K _W	0.4454	0.4554	0.4393	0.5042	0.4762
K _H	0.4889	0.5514	0.4285	1.0588	0.7282
K _{L L}	0.4454	0.4554	0.4393	0.5043	0.4762
Δ H melting (J/g)	66.17	82.60	92.99	56.62	59.13
Δ H crystallization (J/g)	29.03	6.909	5.099	4.84	83.65

The investigation into the structural changes resulting from the SiO₂ content in the PbO₂ matrix were investigated through FTIR spectroscopy. In Figure 6, the absorption spectra of PbO₂ and SiO₂ oxide powders are presented. The PbO₂ spectrum exhibits two broad bands around 472 and 890 cm^{−1}. The absorption band at 472 cm^{−1} corresponds to the bending vibrations of Pb-O-Pb and O-Pb-O angles within tetrahedral units [PbO₄], while the prominent band at 868 cm^{−1} signifies the stretching vibrations of Pb-O bonds within structural units [PbO₆]. A shoulder observed at 977 cm^{−1} is attributed to the asymmetric stretching vibrations of Pb-O bonds within structural units [PbO₃]/[PbO₄], whereas bands at 662 and 716 cm^{−1} are specific to the stretching vibrations of Pb-O bonds within structural units [PbO₃] and [PbO₄], respectively. The FTIR absorption spectrum of SiO₂ exhibits three bands centered around 471, 802, and 1107 cm^{−1} and a shoulder located at 1203 cm^{−1}. The absorption band at 471 cm^{−1} corresponds to the bending vibrations of Si-O-Si bonds, while the bands at 802–1107 cm^{−1} arise from the symmetric and asymmetric stretching of the Si-O-Si bond. The latter vibration is accompanied by the presence of an intense shoulder located at higher wavenumbers, approximately at 1203 cm^{−1}. The silica structure is described using the terminology Qⁿ, where n denotes the count of bridging oxygen atoms (O_p–bridging oxygen) Si (O_p)ⁿ with n values of 0, 1, 2, 3, 4 from SiO₄ tetrahedra [20].

The degree of disorder in silicate systems depends on the distribution of structural entities of Qⁿ type. The structure of amorphous silica is composed of Q⁴-type entities. Introducing a network modifier results in depolymerization of the structure by converting bridging oxygens into non-bridging oxygens (O_{np}: non-bridging oxygen) [21] transforming the tectosilicate structure (Q⁴) into disilicate structure (Q³), metasilicate structure (Q²), pyrosilicate structure (Q¹), and orthosilicate structure (Q⁰), respectively.

Figure 7 presents the FTIR absorption spectrum of the glassy system xSiO₂·(100-x) PbO₂ recorded within the frequency range of 300–4000 cm^{−1}. The analysis of the FTIR spectrum can be segmented into two sections. The initial section of the FTIR spectrum, in the range of 300–1500 cm^{−1}, includes vibrations of various structural units attributed to the lead network. The second section, located in the range of 1600–4000 cm^{−1}, with less prominent bands, is characteristic of the vibration modes of water molecules, vibration modes of hydroxyl groups (O-H), and adsorbed organic groups from the atmosphere, including bands at 1630, 3438, and 2932 cm^{−1}.

Table 4. FTIR fundamental structural units of PbO₂ [7,8,12,14] and SiO₂ [19–21].

Frequency (cm ^{−1})	Assignment
479	Pb-O-Pb and O-Pb-O angles bending vibrations
430, 490	Si-O-Si bonds bending vibrations (Q ⁴ entity)
662, 850	Pb-O stretching vibrations in [PbO ₄]
716	Pb-O stretching vibrations in [PbO ₃]
770	Bending vibrations of Si-O-Si bonds in pointed oxygens (Q ⁴ entity)
867	Pb-O stretching vibrations in [PbO ₆]
870	Si-O stretching vibrations (Q ¹ entity)
920–980	Si-O-Si asymmetric stretching vibrations (Q ² entity)
970–1100	Pb-O asymmetric deformation vibrations in [PbO ₃]/[PbO ₄] Si-O-Si asymmetric stretching vibrations (Q ³ entity)
1000–1100	Si-O-Si asymmetric stretching vibrations (Q ⁴ entity)
1460	Carbonate groups
1640	Molecular water or hydroxyl
2252	Hydroxyl stretching and Si-OH bending/SiO ₄ vibrations
2800–2980	Asymmetric and symmetric stretching modes of interstitial H ₂ O molecules.
3400–3500	Molecular water

The band located at 672 cm^{−1}, corresponding to the stretching vibrations of Pb-O bonds in [PbO₄] structural units, exhibits heightened intensity as the SiO₂ concentration increases. Meanwhile, the band at 719 cm^{−1}, associated with stretching vibrations of Pb-O bonds in [PbO₃] structural units, shifts towards higher wavenumbers, specifically to 770 cm^{−1}, with the increase in SiO₂ concentration, $x \geq \text{PS5}$, and is attributed to vibrations of Si-O-Si bonds in SiO₄ units. The band centered at 867 cm^{−1}, attributed to stretching vibrations of Pb-O bonds in [PbO₆] structural units, decreases in intensity with the increase in SiO₂ concentration and shifts towards higher wavenumbers, specifically to 870 cm^{−1} (Q¹). Moreover, for samples PS4–PS9, an observable increase in the intensity of bands within the range of 900–1250 cm^{−1} (Q^{2–4}) can be observed.

The band at 978 cm^{−1} is assigned to stretching vibrations of Si-O-Pb bonds (Q²) [20]; the band at 1020 cm^{−1} is associated with asymmetric stretching vibrations of Si-O-Si bonds (Q³), and this band becomes dominant in samples PS8–PS9. The asymmetric stretching vibrations of Si-O-Si bonds (Q⁴), the band at 1150 cm^{−1}, are highly visible starting with sample S5 and increase as the SiO₂ content increases.

The FTIR results confirm the network-forming role of PbO₂ even at high concentrations of SiO₂ and the formation of a SiO₂ network where the distribution of Q_n entities is heavily impacted by the oxide composition of the system.

The ESR spectra, corresponding to the glass system xSiO₂(100-x)·PbO₂ recorded at room temperature, are presented in Figure 8.

As observed in the figure, the ESR spectra consist of distinct absorptions centered at $g \sim 9.7$, $g \sim 4.3$, and $g \sim 2.06$, characteristic of paramagnetic Fe³⁺ ions with electronic configuration 3d⁵, 6S_{5/2} originating from uncontrolled impurities, as well as the raw materials used. The number and position of the ESR transitions specific to Fe³⁺ ions observable in a powder spectrum depend on the local crystalline field symmetry at the ion positions and the existence of possible magnetic interactions between ions.

Thus, the existence of Fe³⁺ ions in the samples can provide information regarding the local structure and reflect the structural transformations occurring within the matrix as the SiO₂ content increases. The resonance line located at $g \sim 9.7$ corresponds to isolated Fe³⁺ ions arranged in rhombic positions, while the one centered at $g \sim 4.3$ is associated with paramagnetic Fe³⁺ ions isolated in tetrahedral and/or octahedral positions with rhombic distortions [22]. The broad resonance peak at $g \sim 2.06$ is due to Fe³⁺ ions with cubic symmetry involved in magnetic coupling, dipolar, and/or super-exchange interactions, with the latter forming magnetic clusters [23–25]. For samples PS0–PS3, the ESR signal at

$g \sim 4.3$ is predominant, with its intensity decreasing linearly as the concentration of PbO_2 in the samples decreases, while the signal at $g \sim 2.06$ remains unchanged. The decrease in the signal at $g \sim 4.3$ can be explained by the decrease in the concentration of Fe^{3+} impurities in the sample. In the case of sample PS4, there is a noticeable decrease in the signal intensity around $g \sim 4.3$ along with a corresponding increase in the signal intensity at $g \sim 2.06$. As the concentration of PbO_2 continues to decrease (and that of SiO_2 increases), the signal at $g \sim 4.3$ maintains a similar intensity to that observed in previous samples, but the ESR signal centered at $g \sim 9.7$ intensifies in samples PS5, PS8, and PS9, respectively, as is that at $g \sim 2.06$ for sample PS6.

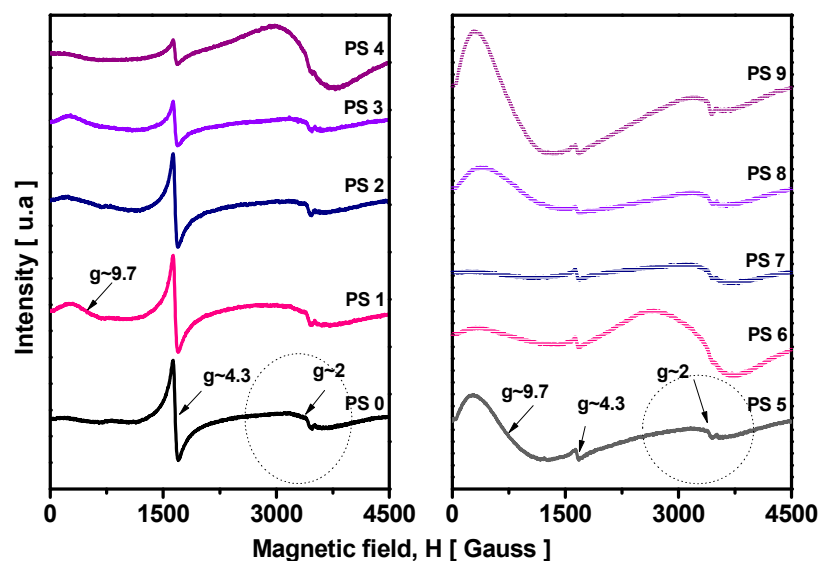


Figure 8. The ESR spectra of the glassy system $x\text{SiO}_2 \cdot (100-x) \text{PbO}_2$.

The evolution of the localization of the ESR signals indicates modifications in the symmetry of the positions occupied by the Fe^{3+} ions as the SiO_2 concentration increases, suggesting the existence of major structural modifications within the matrix. This is correlated with the enhancement in the degree of structural order observed in the XRD analysis. By tracking the evolution of the shape and intensity of the absorption at $g \sim 2.06$, a broadening effect of the signal can be observed in samples PS4 and PS6, suggesting the intensification of dipolar interactions between the Fe^{3+} ions.

4. Conclusions

Lead dioxide glass doped with varying concentrations of SiO_2 was synthesized using the melt-quenching technique at a low temperature. XRD analysis verified the amorphous structure of the investigated samples. The structural changes resulting from the substitution of PbO_2 with SiO_2 , along with their impact on the thermal stability, chemical durability, and structural characteristics of the glass network, were unveiled by combining DSC analysis with ICP-MS, FTIR, and ESR spectroscopy investigations. The free-bubble samples, PS1–PS5, respectively, are a suitable parent glass for development of the new glass crystalline material (GCM) compositions with specific desired properties. The study of the evolution of the structural, thermal, and chemical properties of the new binary network-former system (PbO_2 glass matrix doped with SiO_2) is of interest for both fundamental and applied research.

Author Contributions: Conceptualization, M.Z.; methodology, M.Z.; validation, M.Z. and R.A.M.; investigation, R.C.G., A.A.D., A.P. and R.A.M.; writing—original draft preparation, M.Z., R.C.G., S.M., A.A.D., A.P., M.L.S. and R.A.M.; writing—review and editing, M.Z., R.C.G., S.M., A.A.D., A.P., M.L.S. and R.A.M.; supervision, R.A.M.; All authors have read and agreed to the published version of the manuscript.

Funding: This research was funded by the Ministry of Research, Innovation and Digitization through CNCs–UEFISCDI, project No: PN-III-P1-1.1-PD-2021-0721, within PNCDI III, and through Nucleu Programme within the National Plan for Research Development and Innovation 2022–2027, carried out with the support of MCID, Project No. PN 23 24 02 01.

Data Availability Statement: Data is unavailable due to privacy.

Acknowledgments: This work was financial supported from the Ministry of Research, Innovation and Digitization through CNCs–UEFISCDI, project No: PN-III-P1-1.1-PD-2021-0721, within PNCDI III, and through Nucleu Programme within the National Plan for Research Development and Innovation 2022–2027, carried out with the support of MCID, Project No. PN 23 24 02 01.

Conflicts of Interest: The authors declare no conflicts of interest. The funders had no role in the design of the study; in the collection, analyses, or interpretation of data; in the writing of the manuscript; or in the decision to publish the results.

References

1. Ruzha Harizanova, R.; Mihailova, I.; Cherkezova-Zheleva, Z.; Paneva, D.; Georgieva, M.; Tzankov, D.; Avdeev, G.; Rüssel, C. Glass–crystalline materials with high iron oxide concentration: Phase composition, redox ratio and magnetic properties. *Bol. Soc. Esp. Ceram. Vidr.* **2024**, *63*, 23–32. [\[CrossRef\]](#)
2. Li, M.; Kong, L.; Wang, W.; Ma, Y.; Jiang, H. Microstructure, Dielectric Properties and Bond Characteristics of Lithium Aluminosilicate Glass-Ceramics with Various Li/Na Molar Ratio. *Crystals* **2023**, *13*, 1647. [\[CrossRef\]](#)
3. Ojovan, M.I.; Yudintsev, S.V. Glass, ceramic, and glass-crystalline matrices for HLW immobilization. *Open Ceramics* **2023**, *14*, 100355. [\[CrossRef\]](#)
4. Alzahrani, A.S. A Review of Glass and Crystallizations of Glass-Ceramics. *Adv. Mater. Phys. Chem.* **2022**, *12*, 261–288. [\[CrossRef\]](#)
5. Sosso, G.C.; Chen, J.; Cox, S.J.; Fitzner, M.; Pedevilla, P.; Zen, A.; Michaelides, A. Crystal Nucleation in Liquids: Open Questions and Future Challenges in Molecular Dynamics Simulations. *Chem. Rev.* **2016**, *116*, 7078–7116. [\[CrossRef\]](#) [\[PubMed\]](#)
6. Caurant, D.; Wallez, G.; Majérus, O.; Roisine, G.; Charpentier, T. Structure and Properties of Lead Silicate Glasses. In *Lead in Glassy Materials in Cultural Heritage*; ISTE Wiley: Hoboken, NJ, USA, 2024; Chapter 3, pp. 37–92, ISBN 978-1-394-26540-4.
7. Zagrai, M.; Macavei, S.G.; Gavrea, R.C.; Popa, A.; Dehelean, A.A.; Barbu-Tudoran, L.; Soran, M.-L. Evaluation of the physical, thermal and structural properties of copper-lead glass for efficient incorporation of MoO₃. *J. Alloys Compd.* **2023**, *968*, 172062. [\[CrossRef\]](#)
8. Zagrai, M.; Macavei, G.S.; Popa, A.; Barbu-Tudoran, L.; Gavrea, R.C.; Mereu, A.R.; Soran, M.-L. Structural, thermal and physical properties of cesium doped molybdenum-copper-lead glass. *J. Non-Cryst. Solids* **2023**, *619*, 122577. [\[CrossRef\]](#)
9. Feller, S.; Lodden, G.; Riley, A.; Edwards, T.; Croskrey, J.; Schue, A.; Liss, D.; Stentz, D.; Blair, S.; Kelley, M.; et al. A multispectroscopic structural study of lead silicate glasses over an extended range of compositions. *J. Non-Cryst. Solids* **2010**, *356*, 304–313. [\[CrossRef\]](#)
10. Suresh, B.; Zhydashchevskii, Y.; Brik, M.G.; Suchocki, A.; Srinivasa Reddy, M.; Piasecki, M.; Veeraiah, N. Amplification of green emission of Ho³⁺ ions in lead silicate glasses by sensitizing with Bi³⁺ ions. *J. Alloys Compd.* **2016**, *683*, 114–122. [\[CrossRef\]](#)
11. La Delfa, S.; Ciliberto, E.; Pirri, L. Behaviour of copper and lead as chromophore elements in sodium silicate glasses. *J. Cult. Herit.* **2008**, *9*, e117–e122. [\[CrossRef\]](#)
12. Zagrai, M.; Macavei, S.; Rada, S.; Pică, M.E.; Pruneanu, S.M. Structural and spectroscopic properties of gadolinium-lead-lead dioxide glasses. *J. Non-Cryst. Solids* **2022**, *576*, 121234. [\[CrossRef\]](#)
13. Zagrai, M.; Suci, R.-C.; Rada, S.; Pică, M.E.; Pruneanu, S. Structural and optical properties of Eu³⁺ ions in lead glass for photonic applications. *J. Non-Cryst. Solids* **2021**, *569*, 120988. [\[CrossRef\]](#)
14. Hordieiev, Y.S.; Zaichuk, A.V. Structure, thermal and crystallization behavior of lead-bismuth silicate glasses. *Results Mater.* **2023**, *19*, 100442. [\[CrossRef\]](#)
15. Kohara, S.; Ohno, H.; Takata, M.; Usuki, T.; Morita, H.; Suzuya, K.; Akola, J.; Pusztai, L. Lead silicate glasses: Binary network-former glasses with large amounts of free volume. *Phys. Rev. B* **2010**, *82*, 134209. [\[CrossRef\]](#)
16. Shih, P. Properties and FTIR spectra of lead phosphate glasses for nuclear waste immobilization. *Mater. Chem. Phys.* **2003**, *80*, 299–304. [\[CrossRef\]](#)
17. Rahimi, R.; Sadrnezhaad, S.K. Effects of Ion-Exchange and Hydrolysis Mechanisms on Lead Silicate Glass Corrosion. *Corrosion* **2012**, *68*, 793–800. [\[CrossRef\]](#) [\[PubMed\]](#)
18. Erdogan, C.; Bengisu, M.; Erenturk, S.A. Chemical durability and structural analysis of PbO–B₂O₃ glasses and testing for simulated radioactive wastes. *J. Nucl. Mater.* **2014**, *445*, 154–164. [\[CrossRef\]](#)
19. Nascimento, M.L.F.; Souza, L.A.; Ferreira, E.B.; Zanotto, E.D. Can glass stability parameters infer glass forming ability? *J. Non-Cryst. Solids* **2005**, *351*, 3296–3308. [\[CrossRef\]](#)
20. Todea, M.; Turcu, R.V.F.; Vasilescu, M.; Trandafir, D.L.; Simon, S. Structural characterization of heavy metal SiO₂–Bi₂O₃ glasses and glass-ceramics. *J. Non-Cryst. Solids* **2016**, *432*, 271–276. [\[CrossRef\]](#)

21. Bala, M.; Pawaria, S.; Deopa, N.; Dahiya, S.; Ohlan, A.; Punia, R.; Maan, A.S. Structural, optical, thermal and other physical properties of Bi₂O₃ modified Lithium Zinc Silicate glasses. *Mol. Struct.* **2021**, *1234*, 130160. [[CrossRef](#)]
22. Horea, C.; Rusu, D.; Ardelean, I. Structural investigation of $x\text{Fe}_2\text{O}_3 \cdot (100 - x)[\text{P}_2\text{O}_5 \cdot \text{TeO}_2]$ glass system by FT-IR study and EPR spectroscopy. *J. Mater. Sci. Mater. Electron.* **2008**, *20*, 905–910. [[CrossRef](#)]
23. Ardelean, I.; Ciorcas, F.; Peteanu, M.; Bratu, I.; Ioncu, V. The structural study of Fe₂O₃–TeO₂–B₂O₃–SrF₂ glasses by EPR and IR spectroscopies. *Mod. Phys. Lett. B* **2000**, *14*, 653–661. [[CrossRef](#)]
24. Padlyak, B.V.; Kindrat, I.I.; Kulyk, Y.O.; Hordieiev, Y.S.; Goleus, V.I.; Lisiecki, R. Spectroscopy and photoluminescence of complex lead-silicate glass doped with copper. *Mater. Res. Bull.* **2023**, *158*, 112071. [[CrossRef](#)]
25. Padlyak, B.V.; Kindrat, I.I.; Drzewiecki, A.; Goleus, V.I.; Hordieiev, Y.S. Spectroscopic properties and intrinsic photoluminescence of the un-doped lead borate glasses. *J. Non-Cryst. Solids* **2021**, *557*, 120631. [[CrossRef](#)]

Disclaimer/Publisher’s Note: The statements, opinions and data contained in all publications are solely those of the individual author(s) and contributor(s) and not of MDPI and/or the editor(s). MDPI and/or the editor(s) disclaim responsibility for any injury to people or property resulting from any ideas, methods, instructions or products referred to in the content.